GEOPHYSICS, VOL. 69, NO. 1 (JANUARY-FEBRUARY 2004); P. 97–107, 5 FIGS., 1 TABLE.
10.1190/1.1649379

Crosshole IP imaging for engineering and environmental applications

Andreas Kemna*, Andrew Binley‡, and Lee Slater**

ABSTRACT

Induced polarization (IP) imaging is a promising tool in engineering and environmental studies. Application of this technique for near-surface investigations has previously been limited by incomplete understanding of the physicochemical controls on the IP response, together with a lack of appropriate methods for data inversion. As laboratory studies have shown, description of IP in terms of complex electrical conductivity enables access to various structural characteristics pertinent to practical issues such as subsurface lithology definition, hydraulic permeability estimation, or hydrocarbon contaminant mapping. In particular, analysis in terms of real and imaginary conductivity components offers improved lithological characterization, since surface polarization effects are separated from electrolytic and surface conduction effects. An Occam-type IP inversion algorithm based on complex algebra is described which accounts for these advances in IP interpretation by directly solving for complex conductivity. Results from crosshole applications at two case study sites demonstrate the suitability of the IP imaging approach for subsurface characterization. In the first case study, the imaging results correlate with the observed complex sequence of Quaternary sediments at a waste disposal site. Characterization of the polarizability of these sediments offers significant value in lithological differentiation. In the second case study, the results of IP imaging at a hydrocarbon-contaminated site illustrate the potential of the method in environmental studies. The hydrocarbon location is clearly evident from the IP image, and a markedly different response is observed at an uncontaminated region of the site. By adopting empirical structural–electrical relationships, images of textural and hydraulic properties are estimated as a step toward improved quantitative characterization. The success of the method for these contrasting applications supports further investigation into understanding the physical and chemical processes that control observed IP.

INTRODUCTION

The induced polarization (IP) method is a geophysical tool that has primarily been used for mineral exploration (e.g., Bleil, 1953; Pelton et al., 1978; Fink et al., 1990). However, laboratory studies of measurable IP effects associated with nonmetallic minerals (e.g., Olhoeft, 1985; Vanhala and Soininen, 1995; Börner et al., 1996) have identified numerous potential engineering and environmental applications of IP. Since microgeometry and mineralogy exert a strong control on the IP response, it should be possible to use IP as a tool for lithological discrimination and hydraulic characterization. Another promising environmental application of the IP method is the detection of organic contaminants, notoriously difficult targets for detection using other geophysical methods.

Recent advances in IP instrumentation and modeling algorithms, combined with a better understanding of the physicochemical significance of the IP response, encourages field-scale engineering and environmental applications of the method. Within the last 10 years, significant advances in the resistivity method occurred with the development of multielectrode, automated data acquisition systems and 2D (recently 3D) inversion algorithms for resistivity image reconstruction (e.g., Park and Van, 1991; Sasaki, 1994; LaBrecque et al., 1996). Engineering and environmental applications of the resistivity method escalated as a result of these technological advances, which facilitate visualization of the subsurface resistivity distribution. In recent years, this technology has been extended to upgrade the IP method. Instrumentation and software now exist (Oldenburg and Li, 1994; Kemna et al., 2000; Li and

Manuscript received by the Editor January 9, 2002; revised manuscript received April 17, 2003.
*Formerly Deutsche Montan Technologie GmbH, 45307 Essen, Germany; presently Agrosphere Institute (ICG-IV), Forschungszentrum Jülich, 52425 Jülich, Germany. E-mail: a.kemna@fz-juelich.de.
‡Lancaster University, Department of Environmental Science, Lancaster LA1 4YQ, United Kingdom. E-mail: a.binley@lancaster.ac.uk.
**Formerly University of Missouri–Kansas City, Department of Geosciences, Kansas City, Missouri 64110; presently Rutgers University, Department of Earth/Environmental Sciences, 195 College Avenue, Newark, New Jersey 07102. E-mail: lslater@andromeda.rutgers.edu.

Oldenburg, 2000), making it possible to obtain 2D or 3D images of the polarizability of the subsurface.

We document two studies conducted to evaluate crosshole IP imaging as a tool in engineering and environmental investigations. These studies address the key identified near-surface applications of the IP method, namely lithological characterization and hydrocarbon detection. We find that, with careful interpretation, IP imaging can improve our understanding of the engineering properties of the subsurface relative to resistivity imaging alone. Adopting empirical structural–electrical relationships, the in-situ assessment of relevant textural and hydraulic properties is possible. However, our studies also indicate that further laboratory data are needed to better understand the effects of microgeometry, mineralogy, fluid chemistry, and saturation on the IP response. Field-scale imaging of lithological variability, hydraulic characteristics, and hydrocarbon distribution appears to be a promising application of the method.

ELECTRICAL PROPERTIES

Complex conductivity σ^* (* denotes a complex term) is expressed in terms of conductivity magnitude $|\sigma|$ and phase φ or by the real σ' and imaginary σ'' components:

$$\sigma^* = |\sigma| e^{i\varphi} = \sigma' + i\sigma'', \tag{1}$$

where $i = \sqrt{-1}$. The real component is a representation of current flow in phase with the applied electric field, while the imaginary component is the displacement of current 90° out of phase with the applied field.

Two pathways for electric charge transfer within a porous medium exist. Electrolytic conduction occurs through fluids in interconnected pore spaces, and surface (interface) conduction occurs within an ionic double layer at the grain–fluid interface. A simple model for the electrical properties of earth materials results from assuming that electrolytic and surface pathways add in parallel (e.g., Marshall and Madden, 1959; Waxman and Smits, 1968; Rink and Schopper, 1974; Vinegar and Waxman, 1984). At low frequencies (i.e., <1000 Hz), the complex conductivity is then given by

$$\sigma^* = \sigma_{el} + \sigma^*_{surf}(\omega) = [\sigma_{el} + \sigma'_{surf}(\omega)] + i\sigma''_{surf}(\omega), \tag{2}$$

where σ_{el} is a frequency-independent volumetric (electrolytic) conductivity of the interconnected pore space and where σ'_{surf} and σ''_{surf} are frequency-dependent real and imaginary components of the complex surface conductivity σ^*_{surf}, respectively (e.g., Vinegar and Waxman, 1984; Börner et al., 1993; Schön, 1996; Lesmes and Frye, 2001). Thus, σ'_{surf} represents interface current flow in phase with the applied electric field, and σ''_{surf} represents interface polarization. Importantly, the measured imaginary conductivity is only a function of the surface conductivity, whereas the real conductivity is a function of both electrolytic and surface conductivity mechanisms. For small polarization effects (typical of nonmetallic environments), from equation (2) it follows that $\varphi(\omega)$, which is measured with field IP instruments, is approximately equal to the ratio of interface polarization to the combined strength of electrolytic and surface conduction:

$$\varphi(\omega) \cong \frac{\sigma''_{surf}(\omega)}{\sigma_{el} + \sigma'_{surf}(\omega)}. \tag{3}$$

This model implicitly assumes that σ_{el} is essentially frequency independent when measured below 1000 Hz.

In general $\sigma^*_{surf}(\omega)$ depends on the interfacial surface area, surface ionic charge density, surface ionic mobility, and interface geometry over which charge is transferred (Vinegar and Waxman, 1984; Revil and Glover, 1998; Revil et al., 1998; Lesmes and Frye, 2001). Ionic charge density and ionic mobility depend on fluid chemistry. However, $\sigma^*_{surf}(\omega)$ in earth materials appears primarily dependent on specific surface area and relatively weakly dependent on fluid chemistry (Vinegar and Waxman, 1984; Börner and Schön, 1995; Revil and Glover, 1998; Lesmes and Frye, 2001; Slater and Lesmes, 2002a). Near-linear relationships between σ''_{surf} and pore space-related internal surface area S_{por} (e.g., Börner and Schön, 1991; Börner et al., 1996), as well as a power law relationship between σ'_{surf} and S_{por} (Schön and Börner, 1985), are reported. Grain diameter is an important parameter defining the interface geometry over which charge is transferred (e.g., Revil and Glover, 1998). Inverse relationships between median or effective grain diameter and σ'_{surf} (Schön and Börner, 1985; Schön, 1996, his Figure 9.35) as well as σ''_{surf} (Slater and Lesmes, 2002b) are observed for unconsolidated sediments. As a result of the strong influence of clay content on both surface area and grain diameter, σ''_{surf} and σ'_{surf} increase with increasing clay content (e.g., Klein and Sill, 1982; Vinegar and Waxman, 1984). Clay mineralogy also affects $\sigma^*_{surf}(\omega)$. The cation exchange capacity (CEC) increases with increasing surface area and surface charge density. Direct relationships between CEC and, respectively, σ''_{surf} and σ'_{surf} are reported (e.g., Vinegar and Waxman, 1984; Börner et al., 1996).

The dependence of σ''_{surf} on surface area, CEC, and grain-size parameters makes the IP method a potentially very useful technique in lithological characterization. Slater and Lesmes (2002a) review how IP measurements can resolve ambiguity in resistivity measurements, which are strongly influenced by the chemistry of the pore fluid, in addition to lithological properties. Electrical estimates of pore space-related surface area permit hydraulic permeability (K) estimation from IP measurements utilizing Kozeny–Carman-based models (Börner et al., 1996; Sturrock et al., 1999; de Lima and Niwas, 2000; Slater and Lesmes, 2002b). Similarly, IP-derived estimates of grain size permit K estimation based on empirical effective grain-size models (Sturrock et al., 1999; Slater and Lesmes, 2002b).

Börner et al. (1996) propose to use the modified Kozeny–Carman equation by Pape et al. (1987),

$$K \approx \frac{475}{F S_{por}^{3.1}}, \tag{4}$$

to electrically estimate K (in darcies) from the formation factor F and the pore space-related internal surface S_{por} (in μm^{-1}). They determine S_{por} from an approximate linear relationship to σ''_{surf} at a reference frequency $\omega_0 = 1$ Hz (Börner and Schön, 1991):

$$S_{por} = a\sigma''(\omega_0), \tag{5}$$

where a is experimentally determined as 0.086 $\mu m^{-1}(\mu S/m)^{-1}$ (Börner et al., 1996).

As an alternative approach for K estimation in saturated unconsolidated sediments, Slater and Lesmes (2002b) use an observed direct relationship between σ'' and effective grain

size, in this case quantified as d_{10} (the grain size at which 10% of the sample weight is finer):

$$d_{10} \approx \frac{500}{\sigma''}, \tag{6}$$

where d_{10} is in μm and σ'' is in μS/m. Under the assumption that grain size exerts the primary control on hydraulic permeability, Slater and Lesmes (2002b) formulate a simple Hazen (1911) type model to estimate K (in darcys) from d_{10} (in μm), as obtained from equation (6), according to

$$K \approx 0.025(d_{10})^{1.3}. \tag{7}$$

Hydrocarbon contaminants modify the chemistry of the grain–fluid interface (Olhoeft, 1985, 1992; Vanhala et al., 1992; Börner et al., 1993). Consequently, IP measurements are sensitive to hydrocarbon contamination, although IP signatures depend on the type of contaminant and whether clay minerals are present or absent (Olhoeft, 1985, 1992; King and Olhoeft, 1989). Field studies show that the electrical signature of a hydrocarbon-contaminated site may also vary with time (e.g., Sauck et al., 1998). Despite the current incomplete understanding of the electrical properties of hydrocarbon-contaminated sediments, applications of IP to contaminated sites are emerging. For example, Daily et al. (1998) image the migration of perchloroethylene in an experimental tank using IP.

IP IMAGING METHOD

Crosshole imaging results were obtained using a complex resistivity inversion algorithm originally proposed by Kemna and Binley (1996) and discussed in detail in Kemna (2000). The algorithm directly solves for conductivity magnitude and phase by consequent adoption of complex calculus. Although the approach is analogously applicable to 3D imaging (Shi et al., 1998; Yang et al., 2000), we assume that the region of interest may be represented as a 2D distribution $\sigma^*(x, z)$. This is considered a fair approximation for the two field cases studied since both sites exhibit a layered sequence of sediments with predominantly vertical rather than lateral conductivity variations. Accordingly, 3D effects in impedance data collected in a vertical image plane at the site are expected to be insignificant.

For low measurement frequencies (typically < 10 Hz), electromagnetic induction effects can be neglected. In this case, the complex resistivity forward problem for a point source at the origin with (zero-phase) current I is defined by

$$\frac{\partial}{\partial x}\left(\sigma^*\frac{\partial \phi^*}{\partial x}\right) + \frac{\partial}{\partial z}\left(\sigma^*\frac{\partial \phi^*}{\partial z}\right) - k^2\sigma^*\phi^* = -\frac{I}{2}\delta(x)\delta(z) \tag{8}$$

(e.g., Weller et al., 1996). Here, k is the Fourier transform variable corresponding to the assumed strike direction y, ϕ^* is the complex electric potential in the Fourier domain, and δ is the Dirac delta function. For given boundary conditions, generally of the form

$$\sigma^*\frac{\partial \phi^*}{\partial n} + \beta^*\phi^* = 0, \tag{9}$$

with n denoting the outward normal and the complex parameter β^* defining the type of boundary, equation (8) is solved by means of the finite-element method (Kemna, 2000). Once the discrete complex potential distribution is calculated for a set of wavenumbers k for each current injection position, inverse Fourier transform and appropriate superposition yields the transfer impedance Z_i^* of any desired electrode configuration. The corresponding (complex) sensitivities S_{ij}^* with respect to the complex conductivities σ_j^* of the individual cells of the finite-element mesh,

$$S_{ij}^* = \frac{\partial Z_i^*}{\partial \sigma_j^*}, \tag{10}$$

are efficiently computed utilizing the principle of reciprocity (Kemna, 2000).

Within the inversion, model vector $\mathbf{m}^*$ and data vector $\mathbf{d}^*$ are defined as

$$m_j^* = \ln \sigma_j^* \quad (j = 1, \ldots, M) \tag{11}$$

and

$$d_i^* = \ln Z_{i,obs}^* \quad (i = 1, \ldots, N), \tag{12}$$

where M is the number of parameters (each consisting of a set of lumped finite elements), N is the number of measurements, and $Z_{i,obs}^*$ is the observed transfer impedance. To overcome inherent nonuniqueness of the tomographic resistivity inverse problem, we apply standard smoothness constrained (Occam) regularization (deGroot-Hedlin and Constable, 1990). The objective function $\Psi(\mathbf{m}^*)$ being minimized in the inversion is composed of the complex L_2-measures of data misfit and model roughness, with both terms being balanced by means of a regularization parameter λ:

$$\Psi(\mathbf{m}^*) = \left\|\mathbf{W}_d^*[\mathbf{d}^* - \mathbf{f}^*(\mathbf{m}^*)]\right\|^2 + \lambda\left\|\mathbf{W}_m\mathbf{m}^*\right\|^2. \tag{13}$$

Here, $\mathbf{f}^*$ is the operator of the forward model, $\mathbf{W}_d^*$ is a complex data weighting matrix, and $\mathbf{W}_m$ is a (real) matrix evaluating the first-order roughness of $\mathbf{m}^*$. To account for horizontally layered environments, appropriate anisotropic smoothing may be imposed by separating $\mathbf{W}_m$ into individual, weighted roughness matrices corresponding to horizontal and vertical directions (e.g., Oldenburg and Li, 1994). The data weighting matrix is given by

$$\mathbf{W}_d^* = \mathrm{diag}\left(\frac{1}{\varepsilon_1^*}, \ldots, \frac{1}{\varepsilon_N^*}\right), \tag{14}$$

with (uncorrelated) complex data errors defined as

$$\varepsilon_i^* = \Delta \ln|Z_i| + \mathrm{i}\Delta\varphi_i, \tag{15}$$

where $\Delta \ln|Z_i|$ and $\Delta\varphi_i$ represent the (independent) errors in log magnitude (resistance) and phase of $Z_{i,obs}^*$. Note that ε_i^* describes a confidence region ellipse in the complex plane around the data point d_i^*.

Minimization of the objective function (13) results in an iterative Gauss-Newton scheme, where, starting with a homogeneous distribution $\mathbf{m}_0^*$, at each step q the complex normal equations

$$\begin{aligned}\left(\mathbf{A}_q^{*H}\mathbf{W}_d^{*H}\mathbf{W}_d^*\mathbf{A}_q^* + \lambda\mathbf{W}_m^T\mathbf{W}_m\right)\Delta\mathbf{m}_q^* \\ = \mathbf{A}_q^{*H}\mathbf{W}_d^{*H}\mathbf{W}_d^*\left[\mathbf{d}^* - \mathbf{f}^*\left(\mathbf{m}_q^*\right)\right] - \lambda\mathbf{W}_m^T\mathbf{W}_m\mathbf{m}_q^*\end{aligned} \tag{16}$$

are solved for a model update $\Delta\mathbf{m}_q^*$ (Kemna and Binley, 1996). Here, H and T denote the Hermitian and transpose matrix,

respectively, and $\mathbf{A}_q^*$ is the complex Jacobian matrix evaluated at the current model $\mathbf{m}_q^*$ according to

$$A_{ij}^* = \frac{\partial f_i^*}{\partial m_j^*} = \frac{\sigma_j^*}{Z_i^*} S_{ij}^*. \tag{17}$$

Details on the solution of equation (16) as well as the implementation of the overall inverse procedure, including choice of the regularization parameter, stopping criterion, and robust error reweighting scheme (LaBrecque and Ward, 1990), are given in Kemna (2000).

CASE 1: DRIGG WASTE DISPOSAL FACILITY (UK)

Background

Crosshole IP surveys have been performed at the Drigg Low Level Radioactive Waste Disposal Site, Cumbria, UK, which is operated by British Nuclear Fuels plc (BNFL). The site is underlain by a complex, heterogeneous sequence of Quaternary sediments, up to 60 m thick in places, which, because of their variability, are difficult to characterize. This complexity is not only attributed to the various glacial and postglacial depositional environments particular to this region of the UK but also to isostatic loading and unloading associated with ice sheet advance and retreat. There is a need to characterize these Quaternary deposits in both a geological and hydrogeological sense for a number of reasons. An important engineering requirement is that both buildings and disposal vaults are appropriately constructed. There is also a need to understand the hydrological processes of the sites to assist in locating long-term monitoring boreholes. Furthermore, a radiological risk assessment for the Drigg site requires formulation of a lithological framework to identify potential flow paths (BNFL, 2000).

Trial pits/trenches and borehole investigations have identified vertical and lateral geological variability at the site, complicating lithological characterization. It is important, therefore, to supplement borehole and trial pit data with a geophysical program to facilitate correlation between boreholes and trial pits. Frequently, a combination of the lithological types is represented within each stratigraphical unit, complicating correlation between data points. Since many of the main units are expected to have significant contrasts in geoelectrical properties, resistivity and IP imaging may define the degree of continuity between boreholes. The objective of the field trials reported here was to ascertain if IP imaging could successfully characterize Quaternary deposits, especially at an operating waste disposal site.

For the investigation two boreholes (labeled BH6124 and BH6125), approximately 15 m apart, were drilled to a depth of 41 m using shell and auger technique. Geological logging revealed a series of sediments classified according to the unit descriptions outlined in BNFL (2000). Table 1 shows the log of each unit for boreholes BH6124 and BH6125 following this classification. Forty-five electrodes were installed in each borehole at 0.8-m intervals over the depth range 5.3 to 40.5 m. A crosshole IP survey was performed in 2000 using the RESECS instrument by GeoServe, with measurements of transfer resistance (dc resistivity) and phase angle (IP) made using a square-wave signal with 2.048 s pulse length. In total, 90 electrodes were used and 2984 dipole–dipole combinations were measured in both normal and reciprocal configurations (for error assessment). Of the 5968 measurements, 2730 ($1365 + 1365$) were used for image reconstruction, the others being considered unreliable because of poor reciprocity of transfer resistance or phase angle, often associate with low observed voltages. Image reconstruction was performed using the inversion algorithm outlined above, employing a parameterization with 841 model cells (660 between boreholes).

Results

Figure 1 shows the crosshole electrical images together with the lithological logs and natural gamma-ray logs for the two boreholes for comparison. Note that gamma-ray logs were not available along the entire borehole, and in borehole BH6124 natural gamma rays were only recorded to approximately 12 m depth. The image of real conductivity (σ') in Figure 1a (nearly identical to conductivity magnitude, as $\sigma' \gg \sigma''$ and thus $\sigma' \cong |\sigma|$) shows consistency with the geological logs in terms of expected conductivities and lateral connectivity of identified units of similar geoelectrical properties. A number of conductivity contrasts are seen which correlate with major identified lithological boundaries, shown in Table 1. Most noticeable is a marked contrast in near-surface clayey units and the underlying unsaturated sands. In addition, the saturated fluvial outwash sands between 16 and 24 m show higher conductivity than the overlying unsaturated sediments. Note also the dramatic reduction in σ' between 11 and 12 m, which coincides with observed (in borehole BH6125) increased gravel content (and presumably improved drainage). Most significant, however, in this example is that σ' fails to differentiate the fluvial sands, glacial sand and gravel, and sandstone units, although the image shows a distinct, continuous, and relatively resistive unit between 34 and 36 m, which forms part of the lower glacial till sequence.

Figure 1b shows the image of imaginary conductivity σ'' between boreholes BH6124 and BH6125. This image of polarizability correlates with the image of σ' but also reveals additional information that allows lithological discrimination. The fluvial sands show an increase in σ'' with saturation (as in the case of σ'), which is consistent with previous models of IP effects (e.g., Vinegar and Waxman, 1984). More significant here, however, is the marked contrast in σ'' between the sands and the sand and gravel units. The high gamma counts in the glacial sand and gravel units indicate reasonably high clay content. It would therefore appear that, in comparison with the sand and gravel units, in the fluvial sands surface conduction is more

Table 1. Summarized geological log of boreholes BH6125 and BH6124.

Unit classification following BNFL (2000)	Approximate depth interval (meters below ground level)	
	BH6125	BH6124
Holocene/recent formation	0—2.0	0—2.0
Lacustrine/fluvial formation	2.0—5.9	2.0—5.8
Pebbly clay formation	5.9—10.7	5.8—10.4
Fluvial outwash formation	10.7—24.5	10.4—24.2
Main diamict formation	24.5—35.9	24.2—35.7
Weathered sandstone	35.9—36.2	35.7—36.0
Ormskirk sandstone formation	36.2—41.2	36.0—40.7

significant because of a reduction in effective grain size, which leads to a net increase in surface area. Note also that the sandstone shows σ'' values similar to the fluvial sand units, which may be a result of similar grain-size characteristics.

In Figure 1c the image of conductivity phase φ shows low values for the near-surface clays as a result of the high ohmic conduction. Similarly, at approximately 25 m depth a slight reduction in phase angle is seen. High phase angles are observed in the sandstone unit at the base of the sequence, indicating high polarization relative to ohmic conduction. Despite these clear contrasts in phase angle, this example illustrates the possible ambiguity that may arise from interpretation based on magnitude and phase angle. Separation into real and imaginary components (as in Figures 1a and 1b) improves lithological discrimination.

The sequence of unconsolidated units at the site shows marked variability in geoelectrical response. When combined with conventional dc resistivity, IP measurements, help distinguish different lithological units. The different IP responses reflect the textural (particle-size distribution, for example), and likely mineralogical, variations between these units resulting from differences in origin and nature of deposition.

CASE 2: FORMER JET FUEL DEPOT (STRASBOURG-ENTZHEIM, FRANCE)

Background

In addition to lithological characterization, we illustrate the potential of IP imaging for hydrocarbon detection. Moreover, we demonstrate how quantitative textural and hydraulic information may be inferred from electrical images by adopting empirical structural–electrical relationships. The site is a kerosene-contaminated military site near the Strasbourg-Entzheim airport in France. Principal contamination of the site occurred from 1957 until the early 1970s when it operated as a jet fuel depot. Besides occasional spillage accidents during pumping and other transport operations, which may have caused massive short-term releases of jet fuel, the subsurface has been continuously contaminated over a long time by slowly leaking underground storage tanks and pipelines.

Geologically, the area is characterized by a sequence of fluvial sediments associated with the nearby Rhine and Bruche rivers. A sketch of the stratigraphic situation at the site, as inferred from recent drillings, is included in Figure 2. Below a top loess layer, about 1.5 m thick, follow sands and gravels in which, at a depth of approximately 9 m, a nearly 1-m-thick clayey silt layer is embedded. The groundwater table at the site is subject to seasonal fluctuations up to a magnitude of 1 m. During the present study, it was relatively shallow at a depth of 8.6 m, roughly coinciding with the top of the silt layer.

The jet fuel contamination was assumed to have followed the typical migration pattern of a light non–aqueous phase liquid (LNAPL). Generally, an LNAPL moves downward by gravity through the unsaturated zone until it encounters either a low-permeability formation or the groundwater table. Lateral spreading may occur in the direction of dip of the lithological barrier (gravity driven) or in the direction of groundwater flow (hydraulically driven). In the latter case, because of soluble

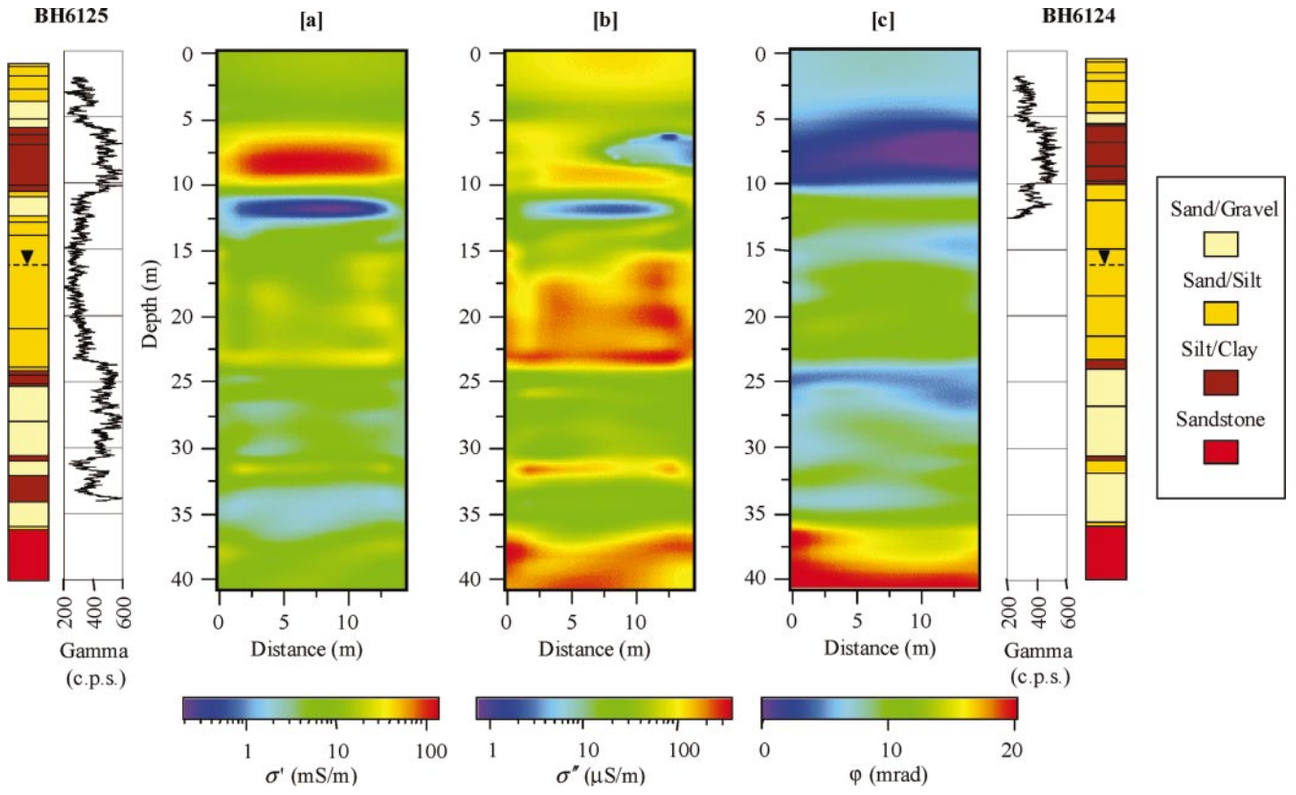

FIG. 1. Crosshole imaging results from Drigg site, showing (a) real component, (b) imaginary component, and (c) phase of complex conductivity. Geological logs and natural gamma-ray logs are shown for comparison. All depths are below ground level.

components, dissolved contaminant plumes may also develop, capable of polluting the groundwater in a large area. An extensive investigation program conducted from 1972 to 1977 and which included the installation of multiple monitoring wells, confirmed such LNAPL movement at this site (Duprat et al., 1979). This study found an area of 400 000 m^2 suffering contamination, with accumulations occurring on top of the low-permeability clayey silt layer, located just above the water table (Figure 2). Mean residual hydrocarbon concentrations in this region were determined as about 1 g/kg. Water sample analyses also proved the presence of dissolved contaminant fractions. Principal constituents included aromatic hydrocarbons such as naphthalene and benzene/toluene/xylene (BTX) with concentrations amounting up to several hundreds of milligrams per liter.

In 1997, Deutsche Montan Technologie (DMT, Germany) conducted resistivity and IP imaging at this site to investigate the practical value of the method for lithological characterization and hydrocarbon detection in a sedimentary environment. For this purpose, several approximately 13-m-deep boreholes were drilled, with each pair of adjacent boreholes (separated by about 8 m) defining a 2D image plane. Sixteen equally spaced electrodes were installed in each borehole, with an electrode separation of 0.75 m. Additional electrodes were placed at the surface between boreholes. Resistance and phase-angle measurements were made using the GDP32-based data acquisition system by Zonge Engineering and Research Organization, Inc. (for system details, see Daily et al., 1996). For each image plane, a variety of dipole–dipole configurations were measured. Resistivity and IP images were calculated using the inversion scheme described earlier. We present selected results that illustrate the value of combined resistivity and IP imaging for understanding lithology and contamination at the site. A more detailed description of the study site and field survey results can be found in Kemna (2000).

For the inversion, the image plane was parameterized into 1131 model cells (735 between boreholes). A total of 612 dipole–dipole data (306 normal + 306 reciprocal), collected at 0.125 Hz frequency, were used for image reconstruction. Individual data error estimates were determined from the differences between corresponding normal and reciprocal measurements.

Results

Electrical images.—Figure 2 shows the inversion result for the selected image plane. The image of real conductivity σ' in Figure 2a basically reflects the lithological stratification at the site. Both the top loess layer and the clayey silt layer at 9 m depth are clearly delineated as conductive features. In contrast, the sand and gravel formations above (unsaturated zone) and below (saturated zone) the silt horizon exhibit, respectively, low and intermediate conductivities. The increase of σ' in the loess and the silt layer must be attributed to surface conduction σ'_{surf} resulting from a relatively high clay mineral content, whereas electrolytic conduction σ_{el} is responsible for the increase of σ' with saturation in the two sand and gravel regions. The image of imaginary conductivity σ'' in Figure 2b shows a similar pattern. Again, the silt unit is characterized by maximum values, indicating highest surface polarization σ''_{surf}

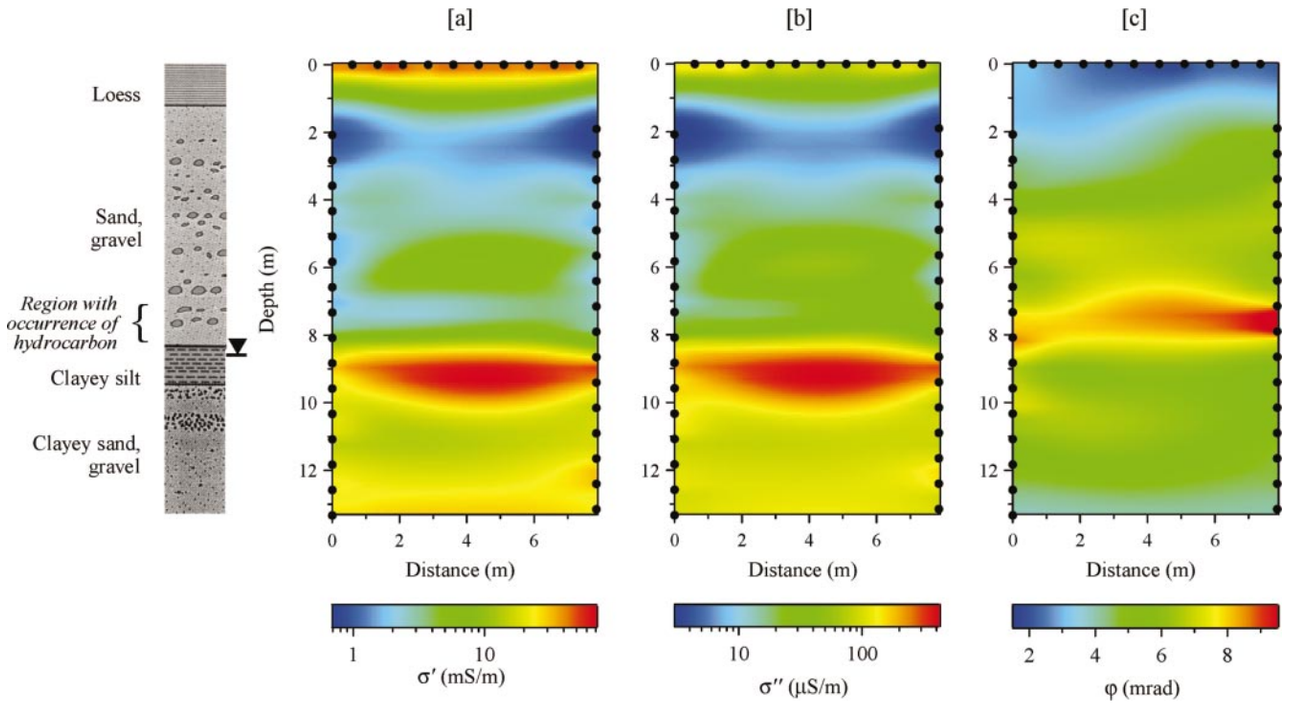

FIG. 2. Crosshole imaging results from the Strasbourg-Entzheim site, showing (a) real component, (b) imaginary component, and (c) phase of complex conductivity. Solid circles indicate position of electrodes. Geological log as determined from cores and occurrence of contamination as proved by chemical sample analyses shown for comparison.

therein. Lowest imaginary conductivities are found in the upper part of the upper sand and gravel region. Neither the real nor the imaginary conductivity image exhibits a significant signature in the region of proved kerosene contamination.

Whereas σ'' represents a direct measure of polarizability, the conductivity phase φ in Figure 2c can be interpreted as a measure of polarizability relative to ohmic conduction. Although, in conjunction with σ' (or $|\sigma|$), both σ'' and φ contain redundant information, the phase image reveals partly different characteristics. Lowest phase shifts occur within the top, clay-rich loess layer, reflecting the dominance of ohmic conduction (Figure 2a) over the yet moderate polarizability (Figure 2b). Importantly, Figure 2c clearly reveals a continuous, roughly 1-m-thick layer of increased phase just on top of the silt horizon (coinciding with a weak resistive anomaly in Figure 2a). The results of chemical core sample analyses indicate that this distinct anomaly coincides with residual hydrocarbon contamination at this depth.

To support this interpretation, a resistivity/IP survey was conducted in an unpolluted area with similar geology upgradient of the military site. The corresponding real and imaginary conductivity results thus serve as control images from a hydrocarbon-free region. As shown in Figure 3b, this reference survey proved the absence of increased phase values directly above the silt layer away from the military site, supporting our theory that the hydrocarbon is responsible for the high phase. However, a different phase behavior is likewise observed within the silt layer itself. Phase shifts at this depth at the contaminated site are significantly smaller than those at the uncontaminated reference site. Therefore, the silt horizon appears to be affected by the contamination as well. This interpretation becomes even more plausible from the corresponding imaginary conductivity curves in Figure 3a. Here, the silt unit coincides with a distinct maximum at the polluted site, which is again absent over the clean underground. The sharp IP effect (phase increase) in the contaminated region above the silt layer in Figure 3b is not evident from σ'' in Figure 3a.

Hydraulic permeability estimation.—We modify the Börner model [equations (4) and (5)] to account for variable water saturation S_w and thus permit hydraulic permeability prediction based on the electrical images from this site. The formation factor F is calculated from an expression given in Börner et al. [1996 their equation (14)], modified to include Archie (1942) saturation dependence:

$$F = \frac{\sigma_w S_w^n}{\sigma' - (\sigma''/\ell)}, \tag{18}$$

where the parameter $\ell = \sigma''_{surf}/\sigma'_{surf}$ accounts for the separation of surface conductivity σ^*_{surf} into real and imaginary parts (Börner and Schön, 1995), and n is the saturation exponent corresponding to σ_{el}. Similarly, we extend the linear relationship between S_{por} and σ''_{surf} found by Börner and Schön (1991) [equation (5)] by incorporating a saturation dependency of σ^*_{surf} according to Vinegar and Waxman (1984):

$$S_{por} = a\frac{\sigma''(\omega_0)}{S_w^{n-1}}, \tag{19}$$

where $n-1$ is the (approximate) saturation exponent corresponding to σ^*_{surf}. The required soil-water characteristic is assumed to follow the simple, two-parameter model

$$S_w(h) = \begin{cases} \left(\dfrac{h}{h_0}\right)^{-1/b}; & h > h_0 \\ 1; & h \le h_0 \end{cases} \tag{20}$$

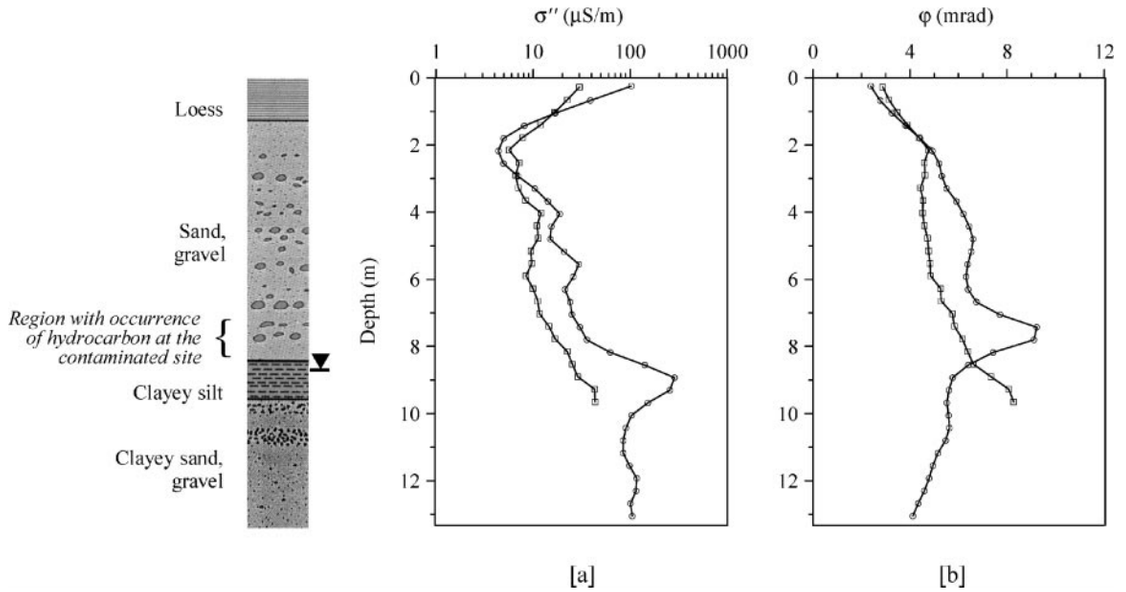

FIG. 3. Vertical distribution of (a) imaginary component and (b) phase of complex conductivity at the contaminated Strasbourg-Entzheim site (circles) and an uncontaminated reference site (squares) as obtained from IP imaging (see Figure 2). At the reference site, exploration depth is less because of a different electrode setup. Geological log and occurrence of contamination are shown for comparison.

(e.g., Cosby et al., 1984), where $h = z - z_{gw}$ is the pressure head (with z_{gw} denoting the groundwater level), h_0 is the height of the capillary fringe, and b is the slope of the retention curve $h(S_w)$ on a double logarithmic plot. For a rough estimation, a more complex soil-water characteristic such as the van Genuchten (1980) model is considered unnecessarily overparameterized. We applied equations (18)–(20) to the IP imaging results of case 2 (Figure 2), choosing the typical values $n \approx 2$ (e.g., Schön, 1996), $l \approx 0.1$ for unconsolidated sediments (Börner et al., 1996), and $b \approx 2.8$ and $h_0 \approx 0.07$ m for sand (Cosby et al., 1984). A mean value of $\sigma_w \approx 108$ mS/m was determined from borehole measurements taken during the IP survey, while the water level was determined as $z_{gw} \approx -8.6$ m. The resultant K estimate image is shown in Figure 4a along with the assumed saturation curve according to equation (20). For comparison, we also applied the model of Slater and Lesmes (2002b) [equations (6) and (7)] based on a simple grain-size approach. This model implicitly assumes saturation. Figure 4b shows the resultant estimated image of effective grain size and hydraulic permeability for field case 2.

Although based on rather weak assumptions, Figures 4a and 4b show that either K estimation model yields valuable additional information. Both images reflect the given sedimentary sequence and its supposed hydraulic characteristics reasonably well. For instance, the clayey silt layer is clearly delineated as a low-permeability unit. Compared to the estimates in the unsaturated sand and gravel zone, the lower K values in the saturated sand and gravel region must be attributed to the presence of a clayey matrix here.

Quantitatively the different models produce relatively similar and, importantly, realistic values for the respective lithological units, differing only slightly with respect to the absolute range (approximately four vs. three orders of magnitude yet with a comparable mean value). This likewise holds for d_{10}, as shown when comparing the granulometric analysis of a core sample (Figure 5) and the estimated mean value in the corresponding region in Figure 4b. Both values are identical to two significant figures, amounting to $d_{10} \approx 3.1$ μm. Although this almost perfect match may be coincidental, it indicates the potential of IP imaging for quantitative assessment of textural characteristics.

The similarity of the K estimate images in Figures 4a and 4b suggests that σ'', as the common input parameter to the applied models, plays the decisive role for K estimation, while F and S_w apparently have less influence. Deviations, however, may be partly attributable to an inherent difference in the approaches. In equations (18) and (19) (Figure 4a), variable saturation is explicitly taken into account, ultimately leading to decreased hydraulic permeability in the unsaturated sand and gravel region (for the chosen parameter values, $K \sim S_w^{1.1}$). In contrast, using equations (6) and (7) (Figure 4b), K estimation is based on effective grain size originally under the assumption of full saturation. Therefore, one might expect to underestimate d_{10}, and thus K, in the saturated zone. However, we believe that, to some extent, this effect compensates for

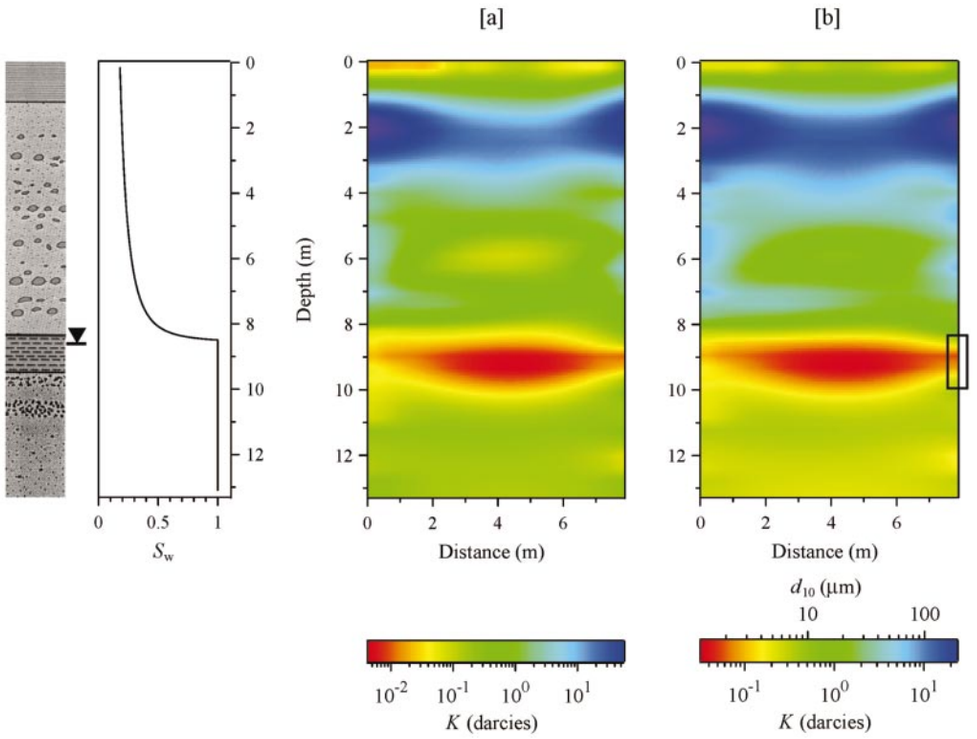

FIG. 4. Distribution of estimated hydraulic permeability in the crosshole image plane at the Strasbourg-Entzheim site as obtained from the complex conductivity result in Figure 2 according to the models of (a) Börner et al. (1996) and (b) Slater and Lesmes (2002b). Geological log and assumed soil-water characteristic for (a) shown for comparison. (b) The rectangle indicates the position of the recovered core sample from the right borehole underlying the granulometric analysis in Figure 5.

the decrease of hydraulic permeability with decreasing water content. In other words, the effective grain size is only associated with the water-filled, interconnected part of the pore space, i.e., that part which actually contributes to the hydraulic (and electrical) conductivity. Finally, note that absolute errors in $\log K$ in Figure 4a may also exist because of an inadequate proportionality constant in equations (5) and (19), which was derived originally for consolidated rather than loose sediments.

Given the model uncertainties in underlying proportionality constants and parameter values such as ℓ and n, the results in Figure 4 should be considered as an order of magnitude K estimate at best. However, this is still of value in many practical situations. For the present case, the estimated K values for the clayey silt layer (up to 10^{-1} darcies in Figure 4b) suggest that it might not represent a long-term hydraulic barrier to water or hydrocarbon transport. This would be in accordance with the actual situation at the site since dissolved contaminant components have been detected in the groundwater below (Duprat et al., 1979).

DISCUSSION AND CONCLUSIONS

The study results illustrate the general value of combined resistivity and IP imaging for improved subsurface characterization. The complementary information provided by recovered conduction and polarization properties helps us to differentiate lithological units and, for case 2, to understand hydrocarbon contamination. At the first site a complex lithology containing fluvial and glacial sediment types as well as bedrock was studied to assess the usefulness of IP for lithological differentiation. The polarizability of the sediments, measured as the imaginary conductivity, offers improved definition of lithological units in comparison with conventional dc resistivity. Whereas the real conductivity is a function of both electrolytic and surface conductivity terms, the imaginary conductivity is predominantly a measure of surface conductivity and thus is well correlated with lithology. The phase angle is a ratio of the imaginary and real conductivity and hence depends on both electrolytic and surface conductivity terms.

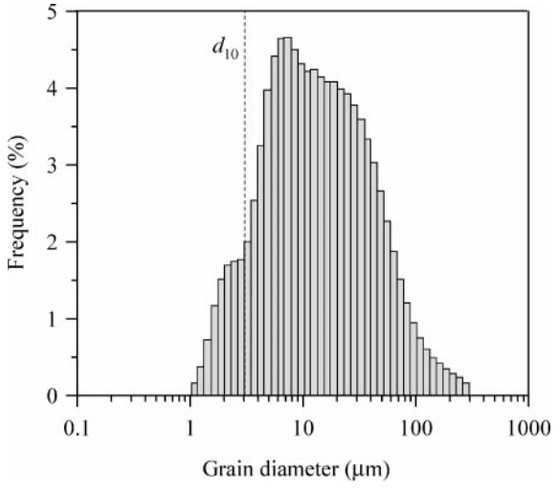

FIG. 5. Granulometric analysis of a fully recovered core sample approximately corresponding to the clayey silt layer (for the exact position, see Figure 4b). The dashed line indicates the grain size with a cumulative frequency on a logarithmic scale of 10%.

While the qualitative association of electrical properties with lithology type is an important achievement, in many situations explicit knowledge about structural properties is needed. To illustrate the significant potential of IP imaging in this respect, for case 2 we attempted a more quantitative interpretation in terms of textural and hydraulic characteristics by adopting empirical structural–electrical relationships and models for K prediction. We used a previously reported empirical correlation between grain size and imaginary conductivity to estimate the spatial distribution of grain size between boreholes. Comparison of electrically estimated grain size with that obtained from sampling correlated a surprisingly well. Using two models to estimate hydraulic permeability from IP measurements provided essentially identical results, suggesting that order of magnitude estimates are obtainable.

Our second study also highlights the potential value of IP imaging for detecting hydrocarbon contaminants. Contaminant detection and monitoring technologies are essential at any facility where hydrocarbons are stored and transported. The image of conductivity phase angle, a measure of polarizability relative to ohmic conduction, resolves the region of proved hydrocarbon contamination, suggesting that phase angle may be an important indicator of the presence of hydrocarbon contamination, although much work is still required to determine the influence of hydrocarbon concentration and chemistry on the IP response. Since observed contamination at this site is high, care must be taken in assuming any generality of this IP signature. The sensitivity of the IP response to contamination level is clearly important and must remain site specific. Nevertheless, the use of the technique as an aid in supporting conventional hydrochemical logging shows obvious potential. We conclude that presentation of IP imaging data should include real conductivity, imaginary (surface) conductivity, and phase angle images.

Our examples' IP analysis was restricted to a single measurement frequency. Yet, the IP response of sedimentary rocks may vary noticeably as frequency of the applied waveform changes. In recent years, numerous laboratory studies have shown that this spectral IP behavior bears significant potential for an improved structural characterization (e.g., Börner et al., 1993; Vanhala, 1997; Sturrock et al., 1999). The described IP inversion scheme, if applied to multifrequency data, provides the possibility to utilize this potential in imaging applications (Kemna et al., 1999, 2000). However, analysis of spectral IP phenomena is beyond the scope of this paper.

Recent advances in multielectrode instrumentation, together with new inversion modeling tools, make crosshole IP imaging feasible for high-resolution subsurface characterization. Interpretation of the modeled IP response is not trivial, but analysis in terms of real and imaginary components of electrical conductivity appears to offer insight into the physical and chemical characteristics of the subsurface environment. The IP inversion scheme described here, directly solving for complex conductivity rather than, for instance, chargeability, can provide these data. Importantly, by the subsequent adoption of empirical structural–electrical relationships, the in-situ assessment of textural and hydraulic properties such as effective grain size and hydraulic permeability, relevant in many

practical situations (e.g., for groundwater model calibration), seems possible.

ACKNOWLEDGMENTS

The work at Drigg was carried out under contract A813613 between Lancaster University and BNFL. Rob Gordon and Matthew Randall (BNFL, Risley) are acknowledged for their support with this work. Peter Winship (Lancaster University) helped with data collection at Drigg. The application of IP at the Strasbourg-Entzheim site was part of a research project supported by the European Environment and Climate Program (contract ENV4-CT95-0079). We are grateful to Deutsche Montan Technologie GmbH (DMT), Essen, Germany, for approval to present selected field results in this paper. The Institut Français du Pétrole (IFP), Paris, kindly provided the results of the granulometric analysis. Finally, we are grateful to the anonymous reviewers, whose constructive comments helped to improve the manuscript.

REFERENCES

Archie, G. E., 1942, The electrical resistivity log as an aid in determining some reservoir characteristics: Transactions of the American Institute of Mining and Metallurgical Engineers, **146**, 54–62.

Bleil, D. F., 1953, Induced polarization: A method of geophysical prospecting: Geophysics, **18**, 636–661.

BNFL, 2000, Status report on the development of the 2002 Drigg post-closure safety case: British Nuclear Fuels plc Report, March.

Börner, F. D., and Schön, J. H., 1991, A relation between the quadrature component of electrical conductivity and the specific surface area of sedimentary rocks: The Log Analyst, **32**, 612–613.

——— 1995, Low frequency complex conductivity measurements of microcrack properties: Surveys in Geophysics, **16**, 121–135.

Börner, F. D., Gruhne, M., and Schön, J. H., 1993, Contamination indications derived from electrical properties in the low frequency range: Geophysical Prospecting, **41**, 83–98.

Börner, F. D., Schopper, J. R., and Weller, A., 1996, Evaluation of transport and storage properties in the soil and groundwater zone from induced polarization measurements: Geophysical Prospecting, **44**, 583–601.

Cosby, B. J., Hornberger, G. M., Clapp, R. B., and Ginn, T. R., 1984, A statistical exploration of the relationships of soil moisture characteristics to the physical properties of soil: Water Resources Research, **20**, 682–690.

Daily, W. D., Ramirez, A. L., and Johnson, R., 1998, Electrical impedance tomography of a perchloroethylene release: Journal of Environmental and Engineering Geophysics, **2**, 189–201.

Daily, W. D., Ramirez, A. L., and Zonge, K., 1996, A unique data acquisition system for electrical resistance tomography: Symposium on the Application of Geophysics to Engineering and Environmental Problems, Environmental and Engineering Geophysical Society, Proceedings, 743–751.

deGroot-Hedlin, C., and Constable, S. C., 1990, Occam's inversion to generate smooth, two-dimensional models from magnetotelluric data: Geophysics, **55**, 1613–1624.

de Lima, O. A. L., and Niwas, S., 2000, Estimation of hydraulic parameters of shaly sandstone aquifers from geoelectrical measurements: Journal of Hydrology, **235**, 12–26.

Duprat, A., Simler, L., and Valentin, J., 1979, Contamination de la nappe phréatique par les hydrocarbures à Entzheim, *in* Duprat, A., Simler, L., and Valentin, J., Eds., Nappe phréatique de la plaine du Rhin en Alsace: Louis Pasteur University of Strasbourg, Mémoire **60**, Science Géologique, 201–216.

Fink, J. B., McAlister, E. O., Sternberg, B. K., Wieduwilt, W. G., and Ward, S. H., Eds., 1990, Induced polarization: Society of Exploration Geophysicists.

Hazen, A., 1911, Discussion of "Dams on sand foundations": Transactions of the American Society of Civil Engineers, **73**, 199.

Kemna, A., 2000, Tomographic inversion of complex resistivity—Theory and application: Ph.D. thesis, Bochum University.

Kemna, A., and Binley, A., 1996, Complex electrical resistivity tomography for contaminant plume delineation: 2nd Meeting on Environmental and Engineering Geophysics, Environmental and Engineering Geophysical Society, European Section, Proceedings, 196–199.

Kemna, A., Binley, A., Ramirez, A. L., and Daily, W. D., 2000, Complex resistivity tomography for environmental applications: Chemical Engineering Journal, **77**, 11–18.

Kemna, A., Räkers, E., and Dresen, L., 1999, Field Applications of complex resistivity tomography: 69th Annual International Meeting, Society of Exploration Geophysicists, Expanded Abstracts, 331–334.

King, T. V. V., and Olhoeft, G. R., 1989, Mapping organic contamination by detection of clay-organic processes: Conference on Petroleum Hydrocarbons and Organic Chemicals in Ground Water—Prevention, Detection, and Restoration, National Water Well Association, Proceedings, 627–640.

Klein, J. D., and Sill, W. R., 1982, Electrical properties of artificial clay-bearing sandstone: Geophysics, **47**, 1593–1605.

LaBrecque, D. J., and Ward, S. H., 1990, Two-dimensional cross-borehole resistivity model fitting, *in* Ward, S. H., Ed., Geotechnical and environmental geophysics III: Society of Exploration Geophysicists, 51–74.

LaBrecque, D. J., Miletto, M., Daily, W. D., Ramirez, A. L., and Owen, E., 1996, The effects of noise on Occam's inversion of resistivity tomography data: Geophysics, **61**, 538–548.

Lesmes, D. P., and Frye, K. M., 2001, Influence of pore fluid chemistry on the complex conductivity and induced-polarization responses of Berea sandstone: Journal of Geophysical Research, **106**, 4079–4090.

Li, Y., and Oldenburg, D. W., 2000, 3-D inversion of induced polarization data: Geophysics, **65**, 1931–1945.

Marshall, D. J., and Madden, T. R., 1959, Induced polarization, a study of its causes: Geophysics, **24**, 790–816.

Oldenburg, D. W., and Li, Y., 1994, Inversion of induced polarization data: Geophysics, **59**, 1327–1341.

Olhoeft, G. R., 1985, Low-frequency electrical properties: Geophysics, **50**, 2492–2503.

——— 1992, Geophysical detection of hydrocarbon and organic chemical contamination: Symposium on the Application of Geophysics to Engineering and Environmental Problems, Environmental and Engineering Geophysical Society, Proceedings, 587–595.

Pape, H., Riepe, L., and Schopper, J. R., 1987, Theory of self-similar network structures in sedimentary and igneous rocks and their investigation with microscopical and physical methods: Journal of Microscopy, **148**, 121–147.

Park, S. K., and Van, G. P., 1991, Inversion of pole-pole data for 3-D resistivity structure beneath arrays of electrodes: Geophysics, **56**, 951–960.

Pelton, W. H., Ward, S. H., Hallof, P. G., Sill, W. R., and Nelson, P. H., 1978, Mineral discrimination and removal of inductive coupling with multifrequency IP: Geophysics, **43**, 588–609.

Revil, A., and Glover, P. W. J., 1998, Nature of surface electrical conductivity in natural sands, sandstones, and clays: Geophysical Research Letters, **25**, 691–694.

Revil, A., Cathles, L. M., III, Losh, S., and Nunn, J. A., 1998, Electrical conductivity in shaly sands with geophysical applications: Journal of Geophysical Research, **103**, B10, 23925–23936.

Rink, M., and Schopper, J. R., 1974, Interface conductivity and its implication to electric logging: 15th Annual Logging Symposium, Society of Professional Well Log Analysts, Transactions, 1–15.

Sasaki, Y., 1994, 3-D resistivity inversion using the finite-element method: Geophysics, **59**, 1839–1848.

Sauck, W. A., Atekwana, E. A., and Nash, M. S., 1998, High conductivities associated with an LNAPL plume imaged by integrated geophysical techniques: Journal of Environmental and Engineering Geophysics, **2**, 203–212.

Schön, J. H., 1996, Physical properties of rocks—Fundamentals and principles of petrophysics: Elsevier Science Ltd.

Schön, J. H., and Börner, F. D., 1985, Untersuchungen zur elektrischen Leitfähigkeit von Lockergesteinen—Der Einfluss matrixbedingter Leitfähigkeitsanteile: Neue Bergbautechnik, **15**, 220–224.

Shi, W., Rodi, W., and Morgan, F. D., 1998, 3-D induced polarization inversion using complex electrical resistivities: Symposium on the Application of Geophysics to Engineering and Environmental Problems, Environmental and Engineering Geophysical Society, Proceedings, 785–794.

Slater, L., and Lesmes, D., 2002a, IP interpretation in environmental investigations: Geophysics, **67**, 77–88.

——— 2002b, Electrical-hydraulic relationships observed for unconsolidated sediments: Water Resources Research, **38**, 1213–1225.

Sturrock, J. T., Lesmes, D. P., and Morgan, F. D., 1999, Permeability estimation using spectral induced polarization measurements: Symposium on the Application of Geophysics to Engineering and Environmental Problems, Environmental and Engineering Geophysical Society, Proceedings, 409–416.

van Genuchten, M. T., 1980, A closed-form equation for predicting the hydraulic conductivity of unsaturated soils: Soil Science Society of America Journal, **44**, 892–898.

Vanhala, H., 1997, Mapping oil-contaminated sand and till with the spectral induced polarization (SIP) method: Geophysical Prospecting, **45**, 303–326.
Vanhala, H., and Soininen, H., 1995, Laboratory technique for measurement of spectral induced polarization response of soil samples: Geophysical Prospecting, **43**, 655–676.
Vanhala, H., Soininen, H., and Kukkonen, I., 1992, Detecting organic chemical contaminants by spectral-induced polarization method in glacial till environment: Geophysics, **57**, 1014–1017.
Vinegar, H. J., and Waxman, M. H., 1984, Induced polarization of shaly sands: Geophysics, **49**, 1267–1287.
Waxman, M. H., and Smits, L. J. M., 1968, Electrical conductivities in oil-bearing shaly sands: Society of Petroleum Engineers Journal, **8**, 107–122.
Weller, A., Seichter, M., and Kampke, A., 1996, Induced-polarization modelling using complex electrical conductivities: Geophysical Journal International, **127**, 387–398.
Yang, X., LaBrecque, D. J., Morelli, G., Daily, W. D., and Ramirez, A. L., 2000, Three-dimensional complex resistivity tomography: Symposium on the Application of Geophysics to Engineering and Environmental Problems, Environmental and Engineering Geophysical Society, Proceedings, 897–906.